06

Influence of the sign of the zeta potential of nanodiamond particles on the morphology of graphene-detonation nanodiamond composites in the form of suspensions and aerogels

© M.K. Rabchinskii,[1] A.D. Trofimuk,[1] A.V. Shvidchenko,[1] M.V. Baidakova,[1] S.I. Pavlov,[1] D.A. Kirilenko,[1] Yu.V. Kulvelis,[2] M.V. Gudkov,[3] K.A. Shiyanova,[1] V.S. Koval,[4] G.S. Peters,[5] V.T. Lebedev,[2] V.P. Melnikov,[3] A.T. Dideikin,[1] P.N. Brunkov[1]

[1] Ioffe Institute,
194021 St. Petersburg, Russia
[2] Petersburg Nuclear Physics Institute named by B.P. Konstantinov of National Research Centre „Kurchatov Institute“,
188300 Gatchina, Russia
[3] N.N. Semenov Federal Research Center of Chemical Physics, Russian Academy of Sciences,
119991 Moscow, Russia
[4] Engelhardt Institute of Molecular Biology, Russian Academy of Sciences,
119991 Moscow, Russia
[5] National Research Center „Kurchatov Institute“,
123182 Moscow, Russia
e-mail: trofimuk.ad@mail.ioffe.ru

Received August 25, 2022
Revised October 21, 2022
Accepted October 22, 2022

A new method of using the detonation nanodiamond with positive and negative zeta potential as a spacer for aerogels based on graphene oxide is presented. It is shown that the dosed addition of detonation nanodiamonds' particles to the suspension of graphene oxide hydrosol made it possible to triple the specific surface area of the resulting aerogel compared to graphene oxide aerogel, and this effect is more significant when nanodiamonds with a positive zeta potential are used. It was also shown that aerogels derived from graphene oxide and detonation nanodiamond with a positive zeta potential have a specific morphology with graphene oxide platelets being twisted. This effect is discussed in terms of the change in the average zeta potential of the initial mixtures.

Keywords: two-component systems, carbon materials, colloid chemistry.

DOI: 10.21883/TP.2022.12.55197.208-22

Introduction

Graphene-based aerogels derived from graphene oxide (GO) suspensions [1] by various methods attracted considerable attention of the scientific community due to the combination of a high specific surface area, electrical conductivity, thermal stability, mechanical strength, and adsorption ability [2-4]. Given these features, graphene-based aerogels can be used as sorbents for oil and specific ions [5–7], graphene-based catalysts [8] and highly porous electrodes for the fabrication of supercapacitors [9,10]. However, several fundamental problems remain to be solved in the formation and subsequent use of graphene-based aerogels. The main one is the problem of the graphene layers stacking due to van der Waals interaction, which leads to degradation of the porous structure of aerogels and a significant decrease in the specific surface area [2,11–13]. Because of this factor, the experimentally achieved capacity, as well as the sorption and catalytic activities of graphene aerogels, are significantly lower than theoretically predicted ones [9]. Thus, the prevention of graphene layers stacking is an important milestone in the further improvement of the graphene aerogels properties.

One of the approaches to solve the problem of stacking is the introduction of additional particles into the aerogels structure, the so-called spacers, which prevent the interaction and stacking of graphene layers. Silica and metal nanoparticles, as well as carbon nanostructures, such as carbon nanotubes, fullerenes, and nanodiamonds, can be used as a spacer.

By using various spacers for the fabrication of the graphene oxide-based aerogels, a unique combination of properties of the final material can be obtained, which opens opportunities for a wide application of such structures For example, in the paper [14] the authors added CoS spherical nanoparticles to graphene-based aerogels to improve its electrochemical characteristics. Furthermore, Ref. [15] reports on applying carbon nanotubes as a spacer to manufacture the supercapacitors with a long service life (more than 1000 cycles). In Ref. [16] the authors obtained a composite material suitable for the oxygen electrochemical reduction, and in Ref. [17] the authors reported on producing the adsorbent with magnetic properties.

Nevertheless, there are several general properties that the spacer in the graphene aerogel must exhibit. Firstly, the addition of spacer should not lead to the reduction

of key parameters of the final material, particularly — its specific surface area. Besides, the spacer must be stable in the liquid or gas medium of the aerogel, has a size of about 1−50 nm, and should be easily chemically modified. As mentioned earlier, several types of spacers are used in graphene aerogels. Most of them are coupled to graphene or graphene oxide platelets by covalent bonds or van der Waals forces.

Q. Wang et al. in Ref. [18] suggested that the introduction of hydroxylated nanodiamond particles as such spacer is also a promising strategy to prevent agglomeration of graphene and graphene derivatives. Based on the description of the authors' experiment, it was supposed that nanodiamond and GO particles in this case are covalently bonded. Besides, no aerogel was obtained in the experiment of the authors. In [19] detonation nanodiamond agglomerates were used as spacer to form films based on the reduced graphene oxide and onion-like carbon. The authors' material demonstrated high electrical conductivity (in the range of 7400−20300 S/m) and high specific surface area (420 m^2/g).

However, note that there is one more way to bond graphene and/or graphene oxide platelets and spacer: to create conditions for their heterocoagulation by a simple electrostatic interaction. This phenomenon, in particular, can be observed in mixtures with particles having opposite charge.

Nanodiamonds obtained by the detonation method (detonation nanodiamonds (DND)) and subjected to deagglomeration and purification procedures are smaller than the nanodiamonds in the papers [18,19]. The maximum of the size distribution of DND particles is lies at about 5 nm [20]. The DND surface can also be modified by chemical and physical means. Depending on the solvent, some chemical groups can dissociate in the liquid phase, forming an electric double layer (EDL). When a particle with a EDL moves in a medium, its electrophoretic mobility can be measured, and the difference of potentials between the inner and outer layers of the EDL can be calculated. This value is called the zeta potential. At the same time, note that obtaining of colloidal solutions of DND particles with positive ($\xi+$) or negative (ξ-) zeta potential in an aqueous medium is currently a well-established technology [21,22]. It is the high value of the ξ-potential of DND and GO particles in aqueous medium ($+70 \pm 10$ mV for DND($\xi+$) [21] and -80 ± 10 mV for DND(ξ-) [22] according to the Hückel model; -70 ± 20 mV for GO according to the Smoluchowski model [23]) that governs for the stability of colloidal solutions of such particles. Our decision to choose DND($\xi+$) particles as the spacer for GO platelets is based on the assumed electrostatic interaction between positively charged DND particles and negatively charged GO platelets in the aqueous medium. The addition of DND suspension with a positive zeta potential ($\xi+$) (DND($\xi+$)) to GO suspension should lead to their heterocoagulation, while the addition of DND suspension with negative zeta potential (ξ-) (DNA(ξ-)) should lead to coagulation by van der Waals forces. In this way, composite structures with different types of components bonding can be formed.

In the present paper composites in the forms of suspensions and aerogels acquired from the initial suspension of GO, from a mixture of GO and DND ($\xi+$), and from the mixture of GO and DND (ξ-) were fabricated and examined. The resulting aerogels with the addition of DND particles demonstrate a higher specific surface area compared to the initial GO aerogel. Different morphology of GO-DND($\xi+$) and GO-DND(ξ-) aerogels is shown and explained based on changing the average ξ-potential of the initial mixtures. Besides, it is shown that the morphology and specific area of the obtained aerogels weakly depend on the amount of added DND($\xi+$) nanoparticles.

1. Samples and methods of investigation

1.1. Graphene oxide suspension

Aqueous suspensions of GO were obtained based on the oxidation and exfoliation of graphite by the modified Hummers method [24]. During synthesis and further experiments, ultrasonic treatment of the GO suspension was excluded to prevent the disruption of the GO platelets. The zeta potential of GO particles was measured to be -90 ± 20 mV (Smoluchowski's model). Aqueous suspensions of GO with a concentration of 0.11 wt.% were used in the work.

1.2. Hydrosols of nanodiamond particles

Industrial DND produced by FSUE „SKTB Technolog" was purified from metallic and inert impurities according to the technology described in [20]. The ash content of the purified DND powder was estimated to be < 0.1 wt.%.

A hydrosol of DND(ξ-) particles was obtained by dispersing the corresponding DND particles in deionized water and centrifugation (RCF (Relative Centrifugal Force) $= 1.8 \cdot 10^4$ g, time $= 40$ min) of the initial DND powder preliminarily annealed in air at 430°C for 6 h according to the procedure described in [22]. Electrokinetic potential of obtained particles in hydrosol: -74 ± 5 mV (Hückel model). $C_{\mathrm{DND}(\xi\text{-})} = 1.00$ wt.%. Before use, the obtained hydrosol was subjected to treatment in an ultrasonic bath with operating frequency of 35 kHz for 40 min.

The hydrosol of DND($\xi+$) particles was prepared by similar procedure from the initial DND powder, preliminarily annealed in a hydrogen atmosphere at 600°C for 3 h in accordance with [21]. Zeta potential of obtained particles in hydrosol: $(+70 \pm 6)$ mV (Hückel model). $C_{\mathrm{DND}(\xi+)} = 1.12$ wt.%. Before the use, the resulting hydrosol was also subjected to treatment in the ultrasonic bath with operating frequency of 35 kHz for 40 min.

For both the DND($\xi+$) hydrosol and the DND(ξ-) hydrosol, the maximum in the particle size distribution was 4.5 nm (similar to the distributions published in [20,22]).

Sample preparation details: mass ratio of GO and DND in the sample (mGO/mDND) before and after washing out and number of washing cycles to remove excess of DND

Sample	Initial mass ratio mGO/mDND	Number wash cycles	Approximate mass ratio mGO/mDND after removal of excess DND
GO−DND(ξ-)_[1.25 → 5.0]	1.25	1	5.0
GO−DND(ξ-)_[0.25 → 0.4]	0.25	1	0.4
GO−DND(ξ-)_[0.14 → 0.2]	0.14	1	0.2
GO−DND(ξ+)_[2.5 → 2.5]	2.5	1	2.5
GO−DND(ξ+)_[1.25 → 1.4]	1.25	1	1.4
GO−DND(ξ+)_[0.6 → 0.7]	0.6	1	0.7
GO−DND(ξ+)_[0.4 → 0.4]	0.4	4	0.4
GO−DND(ξ+)_[0.25 → 0.25]	0.25	4	0.25
GO−DND(ξ+)_[0.18 → 0.24]	0.18	7	0.24
GO−DND(ξ+)_[0.14 → 0.25]	0.14	7	0.25

1.3. Composites „graphene-detonation nanodiamond“ in the form of suspensions

To acquire composites in the form of suspensions, aqueous suspensions of GO were mixed with DND(ξ+) or DND(ξ-) hydrosols. To do this, GO aqueous suspension and hydrosol of DND particles with ξ-potential of a certain sign were simultaneously added to a glass with deionized water while stirring constantly. The volume ratios of GO hydrosol and DND hydrosol were selected based on the given mass ratio of GO/DND (mGO/mDND) indicated in the Table. After mixing, the product was additionally stirred for 15 min.

To remove DND particles not bonded to GO particles from the mixture, the obtained samples were centrifuged at the following conditions: $1.8 \cdot 10^4$ g, 10 min for samples GO−DND(ξ+) and $1.8 \cdot 10^4$ g, 20 min for GO−DND(ξ+) samples. The supernatants were removed, and sediments were diluted with deionized water of the same volume after each centrifugation. The number of wash cycles for each sample is shown in the Table. To determine the amount of DND removed from the mixture and the approximate mass ratio (mGO/mDND) after the washing process, the weight of the solid component in the supernatant after its drying was determined. The obtained samples, washed of excess DND, are designated in this paper as GO−DND(ξ-)_[XX→YY] or GO−DND(ξ+)_[XX→YY], where XX — mGO/mDND in the sample before excess DND was removed, YY — mGO/mDND in the sample after excess DND was removed.

1.4. Composites „graphene-detonation nanodiamond“ in the form of aerogels

Composites in the form of suspensions were frozen by extrusion through a medical syringe into liquid nitrogen at a constant rate of 25 ml/h using a Graseby 3150 syringe pump. After freezing, the samples were lyophilized. The resulting samples are designated in this paper as GO−DND(ξ-)_[XX→YY]_aer or GO−DND(ξ+)_[XX→YY]_aer. Afterwards, the samples were placed in a glass ampoule, evacuated, and subjected to stepwise heat treatment, raising the temperature up to 450°C with constant evacuation of the gaseous products of the GO reduction reaction from the ampoule. After heating the samples were cooled to room temperature while maintaining a vacuum in the system. The resulting samples are designated in this paper as GO−DND(ξ-)_[XX→YY]_aer_red or GO−DND(ξ+)_[XX→YY]_aer_red.

1.5. Characterization of the samples

The size distribution of GO in suspensions and in all composites in the form of suspensions was determined by laser diffraction (LD) using a Mastersizer 2000 analyzer (Malvern Panalytical, UK). DND(ξ+) and DND(ξ-) particle sizes in hydrosols were analyzed by dynamic light scattering (DLS) on Zetasizer Nano ZS analyzer (Malvern Panalytical, UK).

The electrophoretic mobility of DND(ξ+), DND(ξ-), GO particles and all composites in the form of suspensions was determined by laser Doppler electrophoresis (LDE) on a Zetasizer Nano ZS analyzer (Malvern Panalytical, UK).

Washing of composites in the form of suspensions from excess of DND was monitored by absorption spectra recorded on a Unico 2800 spectrophotometer (Unico Sys., USA). All measurements were carried out using a quartz cell with the optical path of 10 mm. The procedure for washing off unbound DND was repeated until the optical density of the supernatant became lower than 0.5 at a wavelength of 200 nm (Fig. 1), since DND has a high optical density in the UV range [25,26].

The specific surface area was measured by the BET (Brunauer–Emmett–Teller) method. To do this, the material sample in the amount of 5−10 mg was placed into

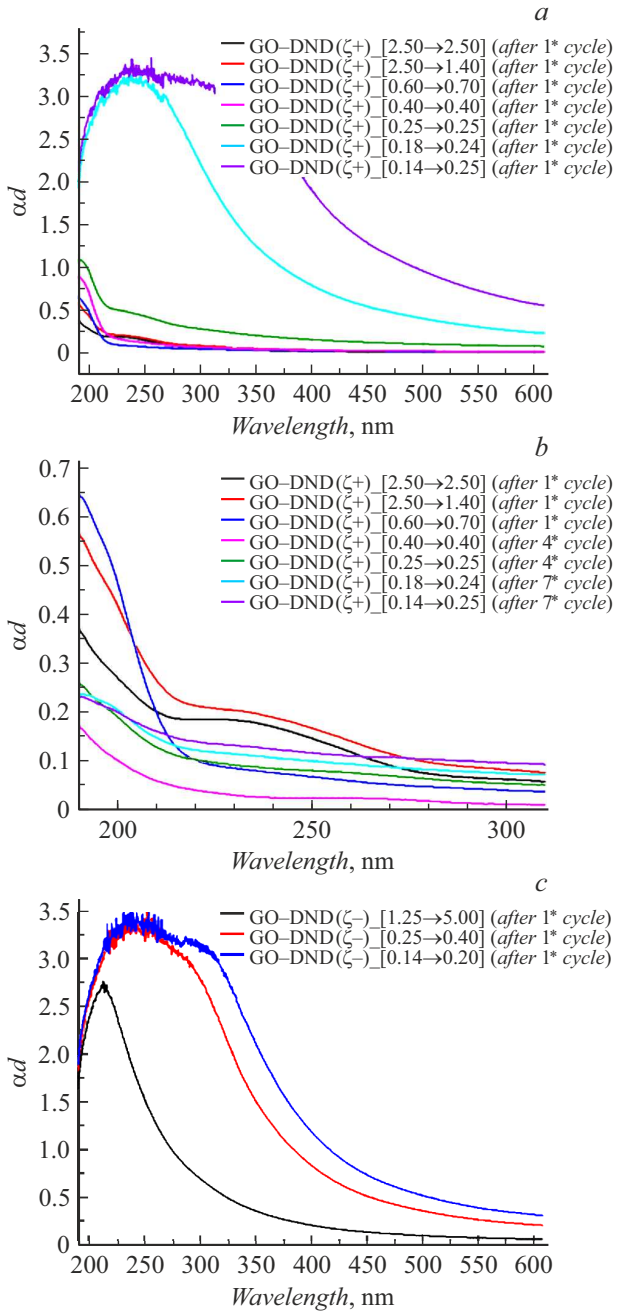

Figure 1. Absorption spectra of supernatants upon removal of excess DND from mixtures of GO−DND($\zeta+$) (*a, b*) and GO−DND(ζ-) (*c*).

the ampoule and pumped out with a vacuum pump to 10^{-2} mm Hg. After that, in order to clean the surface from the adsorbed water and solvent residues, the sample was thermally annealed at $T = 450°$C for 30 min with continuous pumping of desorption products from the heating zone. After heat treatment, the ampoule with the sample was placed in liquid nitrogen, and sorption curves were recorded by periodically puffing a fixed volume of nitrogen into the system, comparing the obtained results with the measurement data of the ampoule without the sample. The obtained data were recalculated to the specific surface area through analysis in the parameters of the BET method.

For studies by transmission electron microscopy (TEM) 30 μl of suspensions of the obtained composites (with a concentration of 0.001 wt.%) were deposited onto copper grids (400 Mesh) using a mechanical pipette dispenser and dried in air within 20 h. TEM images of the studied materials were collected using a Jeol JEM-2100F microscope (Jeol, Japan) with a resolution of 0.19 nm at accelerating voltage of 200 kV.

The morphology of the samples' surface was studied by scanning electron microscopy (SEM) in the secondary electron detection mode using a JSM 7001F scanning electron microscope (JEOL, Japan).

X-ray diffraction studies of aerogels were carried out using a Bruker D2 PHASER diffractometer (Bruker AXS, Germany), made in Bragg–Brentano vertical geometry and equipped with semiconductor linear (1*D*) position-sensitive detector (PSD) LYNXEYE with the opening angle of 5°. The CuK_α radiation from a Bruker X-ray tube with a Cu anode monochromatized by Ni filter (wavelength $\lambda = 0.1541$ nm) was applied. X-ray diffraction patterns were collected in the $\theta-2\theta$ symmetrical scanning mode. To reduce the influence of the possible effect of preferred orientation of crystallites, the sample was rotated around the axis of the sample holder, which coincided with the axis of the goniometer. The X-ray patterns were corrected for zero detector shift and sample displacement effects based on additional measurements using a Si640d X-ray powder standard (NIST, USA)

Small-angle X-ray scattering (SAXS) analysis was performed both for composites in the form of suspensions and for composites in the form of aerogels. The measurements were carried out on the BioMUR beamline (Kurchatov Synchrotron Radiation Source, NRC „Kurchatov Institute", Moscow) [27,28]. The energy of the synchrotron radiation beam on the sample was 8.58 keV (wavelength = 1.445 Å), two unit modes were used (distance from the sample to the detector 1 and 2.5 m), the range of scattering vectors q was 0.04−4 nm^{-1}, which makes it possible to examine the structure in the scale $R \sim 2\pi/q \sim 1.5-150$ nm. Liquid samples were measured in thin quartz capillaries (diameter 1.5 mm, wall thickness 0.01 mm); capillaries filled with solvent (water) were used as background samples. Dry samples (aerogels) were measured between two layers of a polyimide film (kapton); two layers of kapton were also used as a background.

2. Results and discussion

2.1. Investigation of features of mixing GO and DND during the formation of GO−DND(ζ-) and GO−DND($\zeta+$) composites in the form of suspensions

In Ref. [29] it was shown that the laser diffraction method can be used to analyze the size of graphene oxide

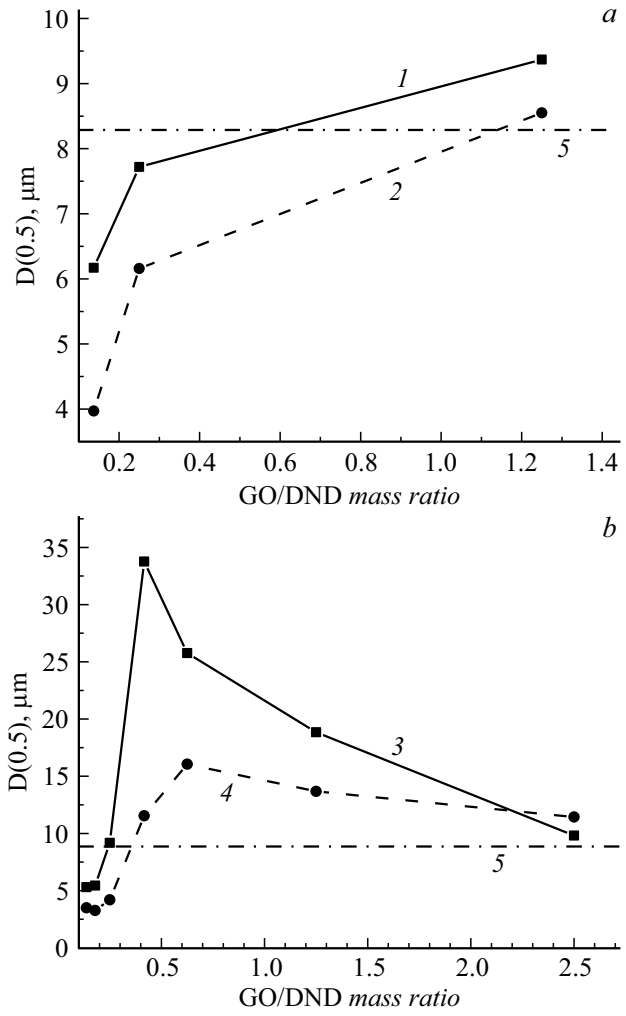

Figure 2. Value of the median $D(0.5)$ of the particle size distribution vs. mass ratio of GO−DND(ξ-) (*a*) and GO−DND($\xi+$) (*b*). The mass ratio is given before removal of excess DND. *1, 2* — GO−DND(ξ-) mixtures before and after removing excess DND, respectively; *3, 4* — mixtures of GO−DND($\xi+$) before and after removal of excess DND, respectively; *5* — GO aqueous suspension.

platelets in water due to their alignment and orthogonal orientation relative to the direction of the propagating radiation. Light scattering from GO particles in this case is determined by diffraction at their edges in accordance with the Fraunhofer light diffraction model. However, the mixing of GO with detonation nanodiamond particles leads to the formation of new structures of a complex shape and with a different orientation relative to the beam, which significantly complicates the interpretation of the results obtained by this method. Nevertheless, analysis of the results obtained allows us to draw some important conclusions regarding the formed structures.

DND(ξ-) particles, like GO, in aqueous medium are characterized by a negative value of ξ-potential. Thus, when mixing DND(ξ-) hydrosol with GO suspension, it is assumed that mutual coagulation of particles should not occur due to the presence of electrostatic repulsion forces between particles. Indeed, the addition of even a significant amount of DND particles (mGO/mDND = 0.14) to a GO suspension does not lead to significant changes in the size of GO particles (Fig. 2, *a*). Nevertheless, there is a tendency for the decrease in the median value $D(0.5)$ with the increase in the mass fraction of DND, which also manifests itself after washing the mixture from the excess of nanodiamond. The decrease in the size of GO particles can be associated with the effect of the charged DND particles on the arrangement of GO platelets in the mixture. When the mixture is washed of the excess of DND, nanodiamond particles co-deposit with GO platelets under the action of centripetal acceleration. Such collective deposition can lead to DND particles binding to each other and to GO platelets due to intermolecular attraction forces (van der Waals forces).

A fundamentally different situation is observed in the interaction of DND($\xi+$) particles with GO, since when DND($\xi+$) is added to GO, the Tindall effect is observed, which indicates mutual coagulation (heterocoagulation) of the particles. With the increase in the mass fraction of DND($\xi+$), the sizes of aggregates grow, reaching several tens of micrometers (Fig. 2, *b*), which is probably due to DND particle binding several GO platelets. Notably, drastic size decrease in the mGO/mDND range from 0.4 to 0.25 can be observed. Such a drop, as follows from the data on the electrophoretic mobility of the structures under study (Fig. 3), is due to that in this range the negative charge of the GO platelets becomes completely compensated by the positive charge of DND at mGO/mDND $\approx$ 0.29. In this case, the electrostatic binding of the GO platelets by means of DND($\xi+$) particles stops. With the increase in the DND mass fraction, the excessive positive charge formed near each plate provides the possibility for large structures to disrupt, probably, even to individual GO platelets, which surface is covered with DND particles in maximum amount. Washing the mixtures from the excess of DND showed that up to mGO/mDND = 0.25 almost complete binding of DND particles to GO platelets is observed (see Table). However, as in the case of GO−DND(ξ-) mixtures, washing leads to decrease in the median size of aggregates (Fig. 2, *b*). Probably, in this case the binding of DND particles to each other occurs due to the van der Waals forces, which ultimately leads to density increasing of the resulting structures.

The analysis of the values of the electrophoretic mobility of the obtained structures (u_e) allows us to state that in the case of GO−DND($\xi+$)_XX mixtures, the negative charge of the GO platelets becomes compensated by the positive charge of the DND($\xi+$) particles, which is characterized by a monotonic decrease of the mobility's absolute value of the formed structures with an increase in the mass fraction of DND($\xi+$) and, ultimately, the sign change of the structure charge at mGO/mDND = 0.29 (Fig. 3). Washing mixtures from the excess of DND($\xi+$) shows that at mass ratio of mGO/mDND > 0.25, almost all nanodiamond particles remains bound to GO platelets,

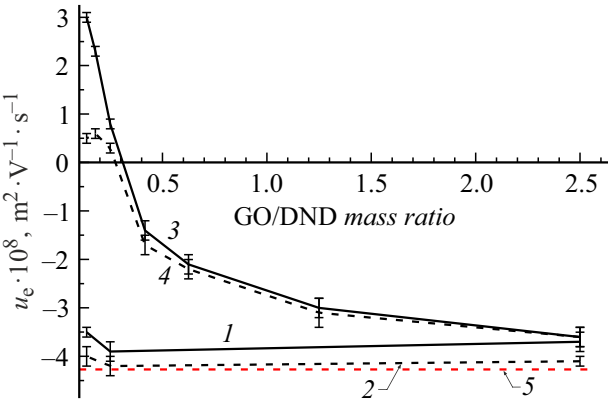

Figure 3. Electrophoretic mobilities of GO−DND($\xi+$)_XX and GO−DND(ξ-)_XX clusters vs. mass fraction of DND particles in mixtures. The mass ratios are given in the calculation before the removal of excess DND. *1, 2* — GO−DND(ξ-) mixtures before and after removing excess DND, respectively; *3, 4* — mixtures of GO−DND($\xi+$) before and after removal of excess DND, respectively; *5* — GO aqueous suspension.

and the electrophoretic mobility of aggregates is fixed at a value close to $0.5 \cdot 10^{-8}$ m^2 V^{-1} s^{-1}. In the case of GO−DND(ξ-) mixtures, the increase in the mass fraction of DND particles in the mixture does not lead to a significant change in the mobility of such structures, and increase in the absolute value of mobility after washing the mixture of excess DND can be associated with the size and shape change of these structures. In this case, it is obvious that to create composites in the form of suspensions, it is most appropriate to use the phenomenon of heterocoagulation of DND($\xi+$) and GO particles in aqueous mixtures. In this case, the limiting mGO/mDND ratio at which complete binding of diamond nanoparticles to GO platelets is observed is 0.24 ± 0.05.

Fig. 4 shows TEM images of samples GO–DND(ξ-)_[XX→YY] and GO−DND($\xi+$)_[XX→YY]. In the case of GO−DND(ξ-) systems this effect is much weaker (Fig. 4, *g, h*) due to mutual repulsion of GO sheets both from each other and from DND(ξ-) particles. The bonding between DND(ξ-) and GO is apparently formed due to the van der Waals interaction. Nevertheless, electrostatic repulsion leads to a less dense distribution of DND(ξ-) over the GO sheet, due to which multilayer graphene inclusions occur in the final composite.

As expected from the analysis of laser diffraction and laser Doppler electrophoresis data, the GO−DND($\xi+$) and GO−DND(ξ-) composites have different nanostructures. In the case of GO−DND($\xi+$), nanodiamond particles are rather uniformly distributed over the surface of the GO platelets both in the case of high and low concentrations. The regions of DND($\xi+$) nanoparticles localization in Fig. 4, *a* correspond to the regions of the maximum concentration of oxygen-containing hydroxyl and epoxy groups involved in electrostatic interaction with positively charged DND($\xi+$) particles. The increase of the concentration and density of nanoparticles after centrifugation is due to the additional binding of nanodiamond particles, now by means of van der Waals forces, to regions of sp^2-hybridized carbon of the GO surface, which are locally preserved after synthesis.

Unlike DND($\xi+$), the spatial distribution of DND(ξ-) nanoparticles has a pronounced heterogeneity with the formation of extended interconnected structures. This configuration corresponds to the geometry of the regions of the non-oxidized GO surface [30,31] — zones of sp^2-hybridized carbon — which is consistent with the assumption about the predominant localization of DND nanoparticles (ξ-) on the GO surface areas free from negatively charged oxygen-containing groups, and adsorption due to van der Waals forces.

2.2. Structure of GO−DND(ξ-) and GO−DND($\xi+$) composites in the form of aerogels

The SAXS curves (dependences of the scattering intensity I on the momentum transfer q) for composites in the form of suspensions are shown in Fig. 5. Samples of suspensions with DND particles with ξ-potentials of different signs were studied. Composites with minimum (mGO/mDND = 5.0 for GO−DND(ξ-) and 2.5 for GO−DND($\xi+$) respectively) and maximum (mGO/mDND = 0.2 for GO−DND(ξ-) and 0.25 for GO−DND($\xi+$), respectively) content of DND particles in the composite relative to GO were compared.

Sample of the initial GO (suspension of initial graphene oxide) has a scattering curve specified by the exponential function (straight line in double logarithmic scales) $I(q) \propto q^{-D}$, which corresponds to scattering from fractal objects [32–34]. The exponent power factor D (slope of the curve) is 2, which corresponds to scattering from the lamellar graphene platelets and indicates their strictly flat structure. All samples containing DND have two exponential ranges with a break at $q \sim 0.7-0.8$ nm^{-1} (corresponds to the scale $R \sim 2\pi/q \sim 8$ nm in a direct space), which coincides with the previously published results of small-angle neutron scattering (SANS) on GO−DND complexes washed of free DND [35].

Previously, it was shown that small-angle scattering from DNDs in suspensions and gels is also characterized by two exponential ranges [36,37]. The range of large q with a slope of 4−4.3 corresponds to primary DND particles, which are smooth objects with sharp edges, and the slope ~ 2.3 at smaller q characterizes clusters of primary DND particles, which are fractal structures in the form of ordered branched chains of DND particles. At the same time, in the scattering patterns of DND suspensions and gels, the boundary between these two regions is at ca. $q \sim 1$ nm^{-1}, which approximately corresponds to the size of these particles $R \sim 2\pi/q \sim 5$ nm.

In our case (for GO−DND composites in the form of suspensions), the kink position shifts to $q \sim 0.7-0.8$ nm^{-1},

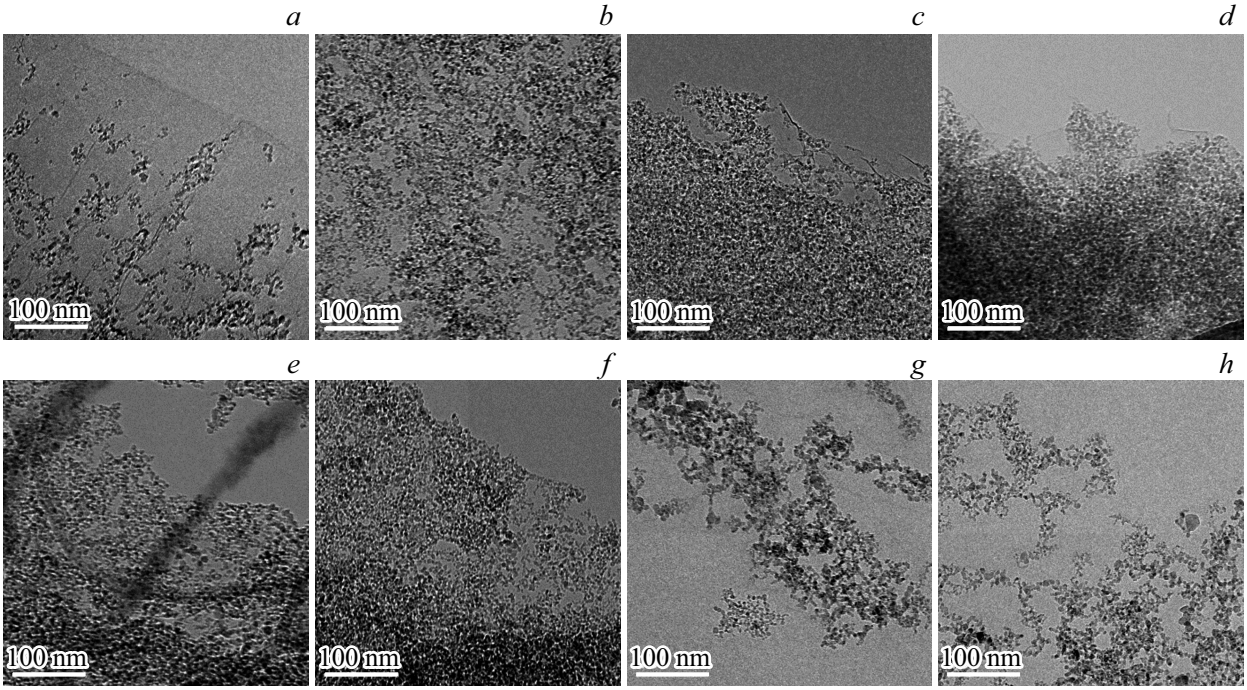

Figure 4. TEM images of air-dried composites in the form of suspensions: GO−DND($\xi+$)_[2.5 → 2.5] before (*a*) and after (*b*) flushing, GO− DND($\xi+$)_[0.25 → 0.25] before (*c*) and after (*d*) washing off, GO−DND($zeta+$)_[0.14 → 0.25] before (*e*) and after (*f*) washing off, GO−DND(ξ-)_[1.25 → 5.0] (*g*) and GO−DND(ξ-)_[0.14 → 0.2] (*h*) after washing off.

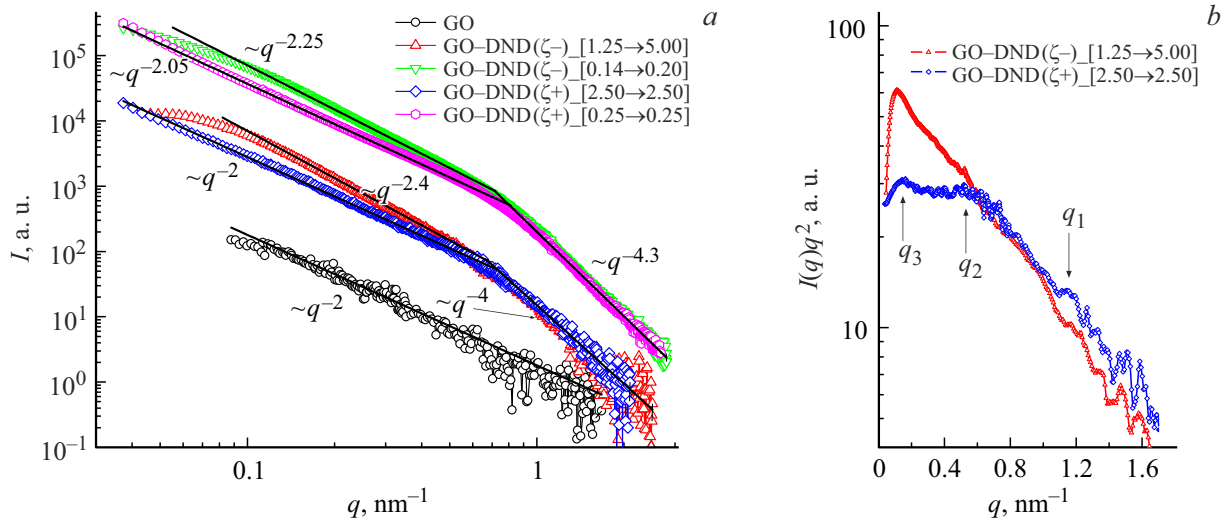

Figure 5. Small-angle X-ray scattering for GO suspension and suspension composites; *a* — scattering intensity $I(q)$: dots — experimental data; straight lines — approximations by the exponential model $I(q) \propto q^{-D}$ with indication of the exponent (slope) D; *b* — data in Kratky representation $I(q)q^2$.

which can be related both to the GO contribution into scattering and to a change in the supraparticle organization of DND particles when they bounds to GO. The range of $q > 0.8\,\text{nm}^{-1}$ has a slope close to 4, as for DND suspensions. At high DND concentrations (samples GO–DND(ξ-)_[0.14→0.2] and GO–DND($\xi+$)_[0.25 → 0.25]), the slope is 4.3, which was repeatedly confirmed earlier by the SANS technique for DND particles in hydrosols. This corresponds to dense particles with sharp edges. Exponential law scattering with $D > 4$ (deviation from Porod's law) usually corresponds to the formation of a diffuse shell on the surface of dense particles (density gradient). Scattering asymptotic is usually represented as $I(q) \sim q^{-(4+2\beta)}$, where β is the diffuseness index of the shell ($0 < \beta < 1$), [33,38]. Note that in a number of papers, when the technology for obtaining isolated 4−5 diamond particles from the batch

of detonation carbon was not yet sufficiently developed, the presence of a non-diamond shell around the diamond core [39] was indicated. However, when explaining the scattering pattern from DND particles in this paper, the interpretation of the exponential slope with $D > 4$ can be more complicated, since it was shown that the thickness of the diffuse shell ($sp^2 + x$-defective phase) for DND ($\xi+$) is minimal [40]. One of the explanations for this effect may be scattering interference from neighboring particles, as shown for DNDs ($\xi+$) in [37]. However, the deviation from Porod's law to the same extent is also observed for DND (ξ-), in which the fraction of $sp^2 + x$-defective phase is noticeably larger, so we cannot exclude the influence of the uncompensated background, which always takes place in the experiment and depends on the concentration [41].

In our GO−DND composites in the form of suspensions, the increase in the slope of this part of the curve in the range 4−4.3 is also observed, as in the case of DND hydrosols and gels, which is associated with scattering from primary particles of DND.

Another reason for the break in the SAXS curve may be due to the GO contribution to scattering. The break in the scattering curves for the GO−DND($\xi+$) complexes at large q was explained in the paper [39] by the thickness of the scattering objects (graphene sheets), and its shift to smaller q — thickening of these formations due to the binding of DND particles and their clusters to individual GO sheets. Apparently, in our composites sticking of DND particles to GO sheets on both sides is also observed, and the thickness of the formed structure becomes about 10 nm.

The range at $q < 0.8\,\text{nm}^{-1}$ allows us to estimate the differences in the structure of the obtained composites of GO with DND(ξ-) and DND($\xi+$) on the scale $\sim 10-100$ nm. Composites with DND(ξ-) (GO−DND(ξ-)_5.0 and GO−DND(ξ-)_0.2) have a higher slope of the curves (2.4 and 2.25) than with DND($\xi+$) (GO−DND($\xi+$)_[2.5 → 2.5] and GO−DND($\xi+$)_[0.25 → 0.25]), whose slope almost strictly remains 2.0. This means that DND($\xi+$) are bound to the graphene oxide sheet and distributed over it rather uniformly without distorting its plane. The GO−DND($\xi+$) system does not contain free DND particles (i.e., all introduced DNDs are bound to GO), so our results coincide with the results [38] for samples with similar mixing conditions: when small amounts of DND($\xi+$) were added to low concentrated GO suspensions, the exponential dependence with a slope of 2 was also preserved. However, with the increase in the DND content and the use of high concentration GO suspensions the authors of paper [38] obtained a curve slope of 2.3 in this area, apparently due to the presence of unbound DND in the system.

DND(ξ-) particles, as expected, bind worse to GO. As can be seen from the Table and Fig. 1, it is impossible to remove free DND(ξ-) particles from suspension composites without material loss (samples GO–DND(ξ-)_[1.25 → 5.0] and GO–DND(ξ-)_[0.14 → 0.2]). And these unbound DND(ξ-) particles are the ones that make a significant contribution to the scattering pattern at $q < 0.8\,\text{nm}^{-1}$, leading to slopes of 2.25−2.4, characteristic for DND suspensions. Deviation from the exponential dependence at the smallest angles ($q < 0.07-0.08$) is also specific for DND hydrosols and gels and is due to the contribution from unbound DND particles (ξ-), which characterizes the next level of DND particles organization in hydrosols, namely, intercluster interaction [39].

Small-angle scattering data for synchrotron radiation demonstrate (Fig. 5, *a*) that the GO−DND(ξ-) and GO−DND($\xi+$) in aqueous suspensions form nanosized and submicron structures with the fractal dimension Df ∼ 2, which is individually characteristic for both graphene oxide in the form of flat sheets of small thickness (1.1 ± 0.2 nm), and for diamonds that tend to organize into chain structures with a dimension close to the indicated one. This makes it possible to use further the Kratky representation and analyze the data in the form of $I(q)q^2$ in order to reveal the features of spatial correlations between components in composites, considering deviations from the $I(q) \sim 1$ dependence dominating in scattering q^{Df} (Fig. 5, *a*). In this representation the results are shown in Fig. 5, *b*, where one can see a significant difference in the scattering patterns for GO−DND(ξ-) and GO−DND composites ($\xi+$) with low DND content.

Negatively charged diamonds are more prone to the formation of nanosized aggregates, as evidenced by an intense peak with a maximum at the position $q_{\max} \sim 0.11\,\text{nm}^{-1}$. As a result, the characteristic size of diamond aggregates is $\sim 2\pi/q_{\max} \sim 60$ nm. In the case of positively charged diamonds, this peak is weakly pronounced, which is explained by the predominant intercalation of diamonds between GO sheets. The peak's shift towards increasing of momentum, $q_{\max} \sim 0.16\,\text{nm}^{-1}$, reflects the size of diamond aggregates decreasing to ~ 40 nm. At the same time, such complexes exhibit a more pronounced wide peak at the position $q_{\max} \sim 0.5\,\text{nm}^{-1}$, which is associated with the interference in scattering at contacts of diamond-graphene assemblies on the corresponding distance ~ 12 nm. This scale corresponds to approximately three sizes of the diamond particle, i.e. the observed object is two GO sheets bounded through DND($\xi+$) diamond particles. The outer surface of such assembly also contains diamond particles with a diameter of $d_P \sim 4.5$ nm, which determines the transverse dimension of the assembly $\sim 3d_P$. Note that negatively charged diamonds also form similar assemblies, but less efficiently, which can be seen from the weakly pronounced enhancement of scattering at scattering vectors $q \sim 0.2-0.8\,\text{nm}^{-1}$ (Fig. 5, *b*). A more detailed data processing made it possible to determine not only the indicated structural characteristics, but also directly confirm that diamonds are spacers between graphene sheets. In Fig. 5, *b*, in addition to peaks at positions q_2, q_3, there is a peak at the value of the scattering vector $q_1 \sim 1.15\,\text{nm}^{-1}$, which corresponds to a scale $\sim 2\pi/q_{\max} \sim 5.5$ nm, exceeding the diamond particle size by ~ 1 nm. It should be concluded that the found value just corresponds to the distance between the GO

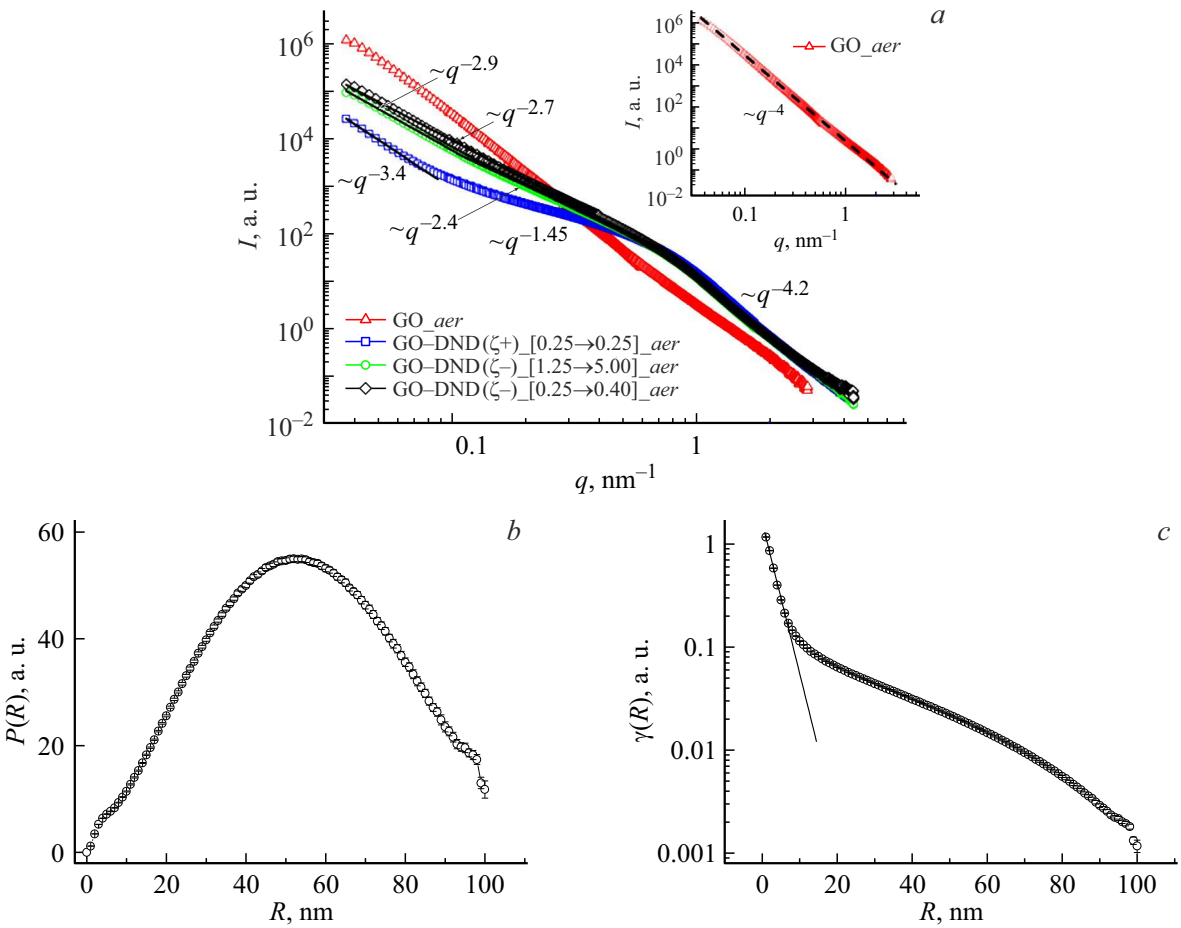

Figure 6. SAXS on composite samples in the form of aerogels; *a* — scattering intensity $I(q)$: dots — experimental data; straight lines — approximations by the power model $I(q) \propto q^{-D}$ with indication of the exponent (slope) D; insert — SAXS for a sample without DND; *b* — distribution function of distances between scattering centers in the sample GO−DND($\xi+$)_[0.25 → 0.25]_aer; *c* — correlation function for sample GO−DND($\xi+$)_[0.25 → 0.25]_aer.

sheets connected through diamonds, $L_1 = d_P + \delta_{GO}$, where $\delta_{GO} \sim 1$ nm is single-layer GO thickness.

2.3. Structure of GO−DND(ξ-) and GO−DND($\xi+$) composites in the form of suspensions

Fig. 6 shows the SAXS curves for GO and GO aerogels with the addition of DNDs. Pure graphene aerogels (insert in Fig. 6) mostly scatter according to the exponential law $I(q) \sim q^{-D}$. The slope of the curve $D = -4$ (corresponds to dense objects with smooth boundaries, Porod's law), smooth deviations from the slope -4 begin only at small angles, which characterizes the size of such dense formations. The GO_aer sample is specified by this dependence up to $q = 0.04-0.05$ nm^{-1} (minimum particle sizes $\sim 120-150$ nm).

For $q > 1$ nm^{-1}, the slope of the SAXS curves for the three studied samples of GO−DNA aerogels is $D \sim 4.2$, which is slightly greater than 4 (Porod's law corresponding to dense particles with sharp edges). Apparently, this region corresponds to the primary dense DND particles 4−5 nm in size, which are part of the aerogel. Exceeding the power of 4 for the slope of this section is presumably due to the interference on the ordered diamond particles, as we have shown above and earlier for DND [36] sols and gels.

On large scales, the GO−DND($\xi+$) structures greatly differ from GO–DND(ξ-) structures. Sample GO–DND($\xi+$)_[0.25 → 0.25]_aer on a scale of 20−60 nm has a section with a slope of -1.45, which corresponds to the common mass fractal with dimension of 1.45 (linear curved chains of particles or also sections with broken surface). On scales 100−150 nm the sample is a surface fractal with fractal dimension $D_s = 6-3.4 = 2.6$.

Samples of the GO−DND(ξ-)_[XX→YY]_aer series have a significantly higher scattering intensity in the small-angle part. Apparently, this is due to the fact that DND particles in such structures are combined into branched chains and bulk clusters, which contribute to scattering (as in DND hydrosols), while in GO−DND($\xi+$) structures DND particles are more isolated and probably distributed almost uniformly on graphene sheets. The scattering curve for the GO−DND(ξ-)_[1.25 → 5.0]_aer sample has slopes 2.4

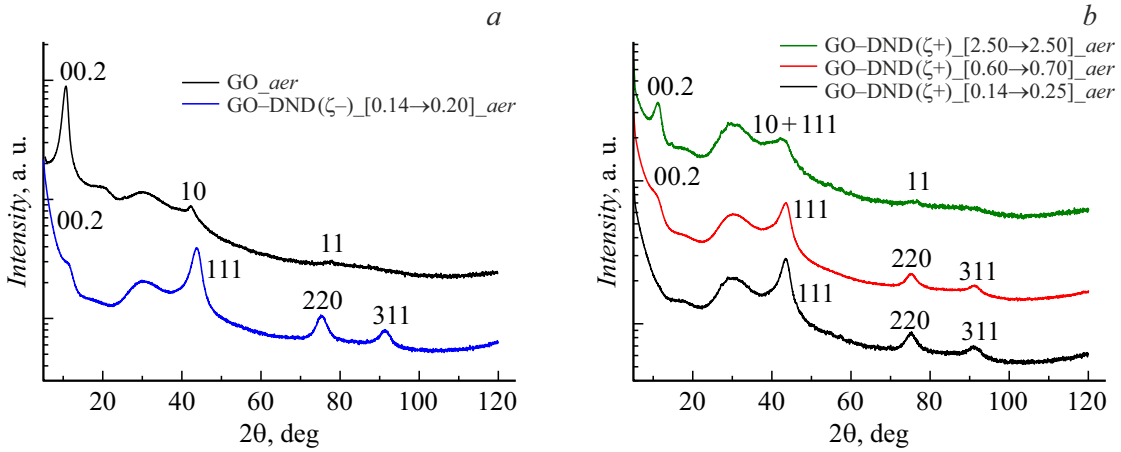

Figure 7. X-ray diffraction patterns of samples of initial GO (a), composite GO−DND(ξ-) in the form of aerogels (b) and also GO−DND($\xi+$) composites in the form of aerogels (a). Next to the peaks, the corresponding Miller indices are given for three-dimensional diffraction (111, 220, and 311), (00.2) for diamond and graphene, respectively, and for two-dimensional diffraction (indices 10 and 11) for graphene. The curves are shifted along the y-axis for clarity.

and 2.9 (mass fractals with corresponding fractal dimensions) with an kink at about 60−80 nm. The sample curve GO−DND(ξ-)_[0.25 → 0.4]_aer on scales 20−150 nm is also a mass fractal (dimension 2.7). Mass fractals in GO aerogels with DND(ξ-) with a dimension close to 3 may mean quite densely filled multilayer structures.

Of greatest interest is the aerogel sample with positively charged diamonds (GO–DND($\xi+$)_[0.25 → 0.25]_aer). For it, using the gnom program of the ATSAS package [43], the function of the distances distribution between scattering centers (Fig. 6, b) was plotted, where a wide main peak is seen with a maximum position, approximately corresponding to the radius of gyration of the detected particles, $R_g = 41.1 \pm 0.1$ nm. At small distances $R \leq 10$ nm a tiny peak is observed against the background of the main peak, which shows correlations of the small radius. The transition to the correlation function $\gamma(R) = P(R)/R^2$ made it possible to determine this radius from the analysis of the spectrum displayed in Fig. 6, c. At small radii, linear behavior of data is observed in logarithmic coordinates depending on the radius, which corresponds to the function $\gamma(R) \sim \exp(-R/R_C)$, where the correlation radius is $R_C = 3.0 \pm 0.1$ nm, which corresponds to the gyration radius of small scattering objects in the present aerogel $R_g = \sqrt{6}R_C \sim 7.3 \pm 0.2$ nm.

The characteristic features of X-ray diffraction of samples of nanosized forms of carbon synthesized from graphite include the following: 1) blurring of the diffraction maxima corresponding to reflections of crystalline graphite; 2) shift of the first maximum towards small angles relative to the 00.2 reflection of graphite; 3) high intensity for two-dimensional diffraction reflections (10 and 11) [43–45]. Fig. 7, a shows the diffraction pattern of the aerogel acquired from the original GO (black curve), which has a narrow peak at the double Bragg angle $2\theta = 11.3°$, which corresponds to diffraction reflection from planes (00.2) with basal distance $d_n = 0.78$ nm. This value corresponds to published data [46]. Besides, one can observe less intense broadened asymmetric peaks at $2\theta = 43°$ and $2\theta = 77.7°$, which are characteristic of 10 and 11 reflections. These peaks appear as a result of two-dimensional diffraction on a flat carbon network of graphene [43].

Diffraction from detonation diamond nanocrystallites was well studied and described in detail in a series of our articles [47]. According to the tabular data, the diffraction curves of diamonds should demonstrate diffraction maxima at the angles $2\theta = 43.9, 75.3, 91.5°$, respectively [48]. Exactly such a set of maxima is observed on the curve for the GO–DND(ξ-)_[0.14 → 0.2]_aer sample (Fig. 7, a, blue curve). From the data of the analysis of the position and half-width of the diffraction maxima, it can be concluded that the dominant phase in the sample under study is the diamond material, which is characterized by the crystal lattice parameter $a = 0.35657 \pm 0.00001$ nm (the identification of the maxima according to the reflection from certain crystallographic planes is shown in the Fig. 7). A detailed analysis of the shape of the diffraction curves and the dependence of the maxima broadening with angle change makes it possible to draw a conclusion about the characteristic size of the coherent scattering region (CSR) in the sample (or about the sizes of crystallites) and microstresses in them. Nanodiamond crystallites in the GO–DND(ξ-)_[0.14 → 0.2]_aer sample are characterized by average particle size with CSR $= 4.5 \pm 0.1$ nm and $e_0 = 0.0019 \pm 0.0001$. Note that for this sample, a shoulder is observed on the scattering curve in the characteristic region for graphene oxide $2\theta = 11.3°$, the appearance of which we attribute to scattering from graphene sheets forming aerogel walls.

The position of the observed features in the $2\theta = 15−35°$ range can be distorted by background scattering from the cell. However, if the maximum at $2\theta = 30°$ remains

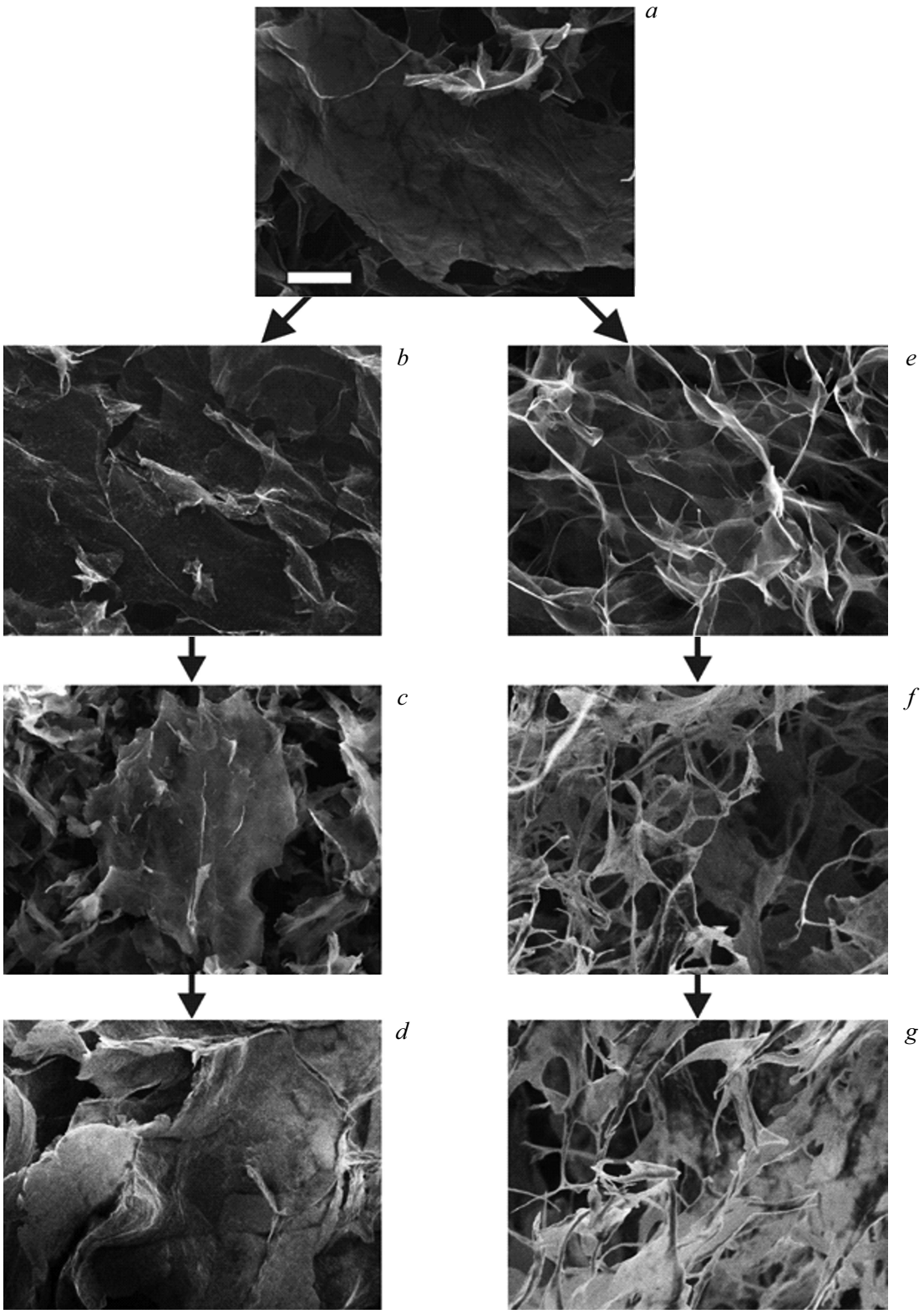

Figure 8. SEM images of composites in form of aerogel: *a* — sample GO_aer; *b, c, d* — samples GO−DND(ξ-)_[1.25 → 5.0]_aer, GO−DND(ξ-)_[0.25 → 0.4]_aer and GO−DND(ξ-)_[0.14 → 0.2]_aer respectively; *e, f, g* — samples GO−DND(ξ+)_[2.5 → 2.5]_aer, GO−DND(ξ+)_[0.4 → 0.4]_aer and GO−DND(ξ+)_[0.18 → 0.24]_aer respectively. The scale mark for all images is shown in Fig. 8, *a* and corresponds to the size of $10\,\mu$m.

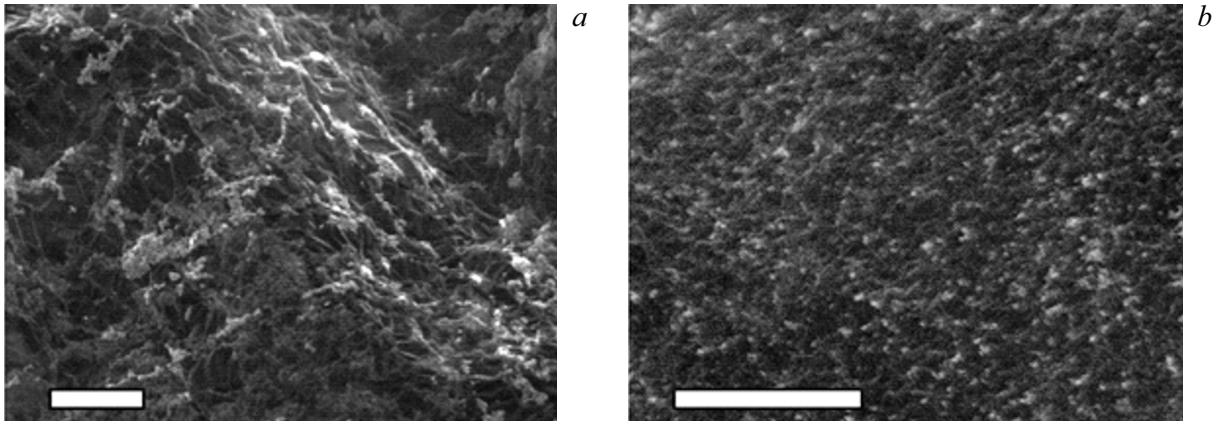

Figure 9. SEM images of composites in form of aerogel: *a* — GO−DND(ξ-)_[1.25 → 5.0], *b* — GO−DND(ξ+)_[2.5 → 2.5]. The scale mark corresponds to the size of 1 μm.

unchanged in its position and intensity for all samples, which indicates that it belongs to scattering from the cell, then the fact that the intensity of the maximum at $2\theta = 18^\circ$ changes indicates the presence of some features in the structure of the sample. The presence of such a maximum can be explained both by scattering from graphite nanoparticles, which may be present in the initial suspension of graphene oxide, and by scattering from those areas in the aerogel that form the corners and joints of its walls. The first version is more probable, since the presence of such particles was already observed in the final product of graphene oxide synthesis [49].

Fig. 7, *b* shows X-ray diffraction patterns for GO/DND aerogels with different DND(ξ+) contents from the maximum, characterized by mGO/mDND(ξ+)=0.25, to the minimum at mGO/mDND(ξ+) = 2.5. The analysis of the maxima corresponding to diffraction by diamond particles makes it possible to estimate their structural parameters: $a = 0.35758 \pm 0.00001$ nm, CSR $= 4.7 \pm 0.1$ nm and $e_0 = 0.0033 \pm 0.0001$, i.e. DND particles in aerogels practically do not differ in structure. On the diffraction patterns of these samples, one can detect characteristic features that appear as a result of scattering from GO sheets and nanodiamond particles, and their intensity depends on the content of DND particles in the sample (i. e., on the mass ratio). Thus, for the GO–DND(ξ+)_[2.5 → 2.5]_aer sample, maximum is clearly visible at $2\theta = 11^\circ$, and no maxima appear at angles typical for 220 and 311 diamond reflections. The asymmetric shape and the shift of the maximum at $2\theta = 43^\circ$ towards smaller angles allows us to consider it as a superposition of diamond reflection 111 and graphene reflection 10. Note that although the content of DND in this sample is low, the intensity of the graphene peak 00.2 is significantly weakened (compared to the aerogel sample without DND), although the peak 10 appears quite clearly. This fact indicates a greater distortion of the packing (stacking, mutual arrangement) and planarity of graphene oxide sheets in comparison with the pure aerogel sample. For the GO–DND(ξ+)_[0.4 → 0.4]_aer sample, a shoulder in the scattering curve is still observed in the $2\theta = 11^\circ$ region, while for the GO–DND(ξ+)_[0.14 → 0.25]_aer sample in the indicated range $2\theta = 10-23^\circ$ no features are observed. This means that with such mass ratio mGO/mDND(ξ+) all graphene sheets are separated from each other. Note that for composite in the form of aerogel GO–DND(ξ-)_[0.14 → 0.2]_aer, even with a higher content of DND particles, the shoulder in the scattering pattern by $2\theta = 11^\circ$ is still observed, and its intensity is comparable to that of the GO–DND(ξ+)_[0.4 → 0.4]_aer sample. This fact correlates well with the TEM data (Fig. 4)

At the macroscale, the aerogel composites obtained by lyophilization are structurally similar to the aerogels studied, for example, in [18]. SEM images of aerogel samples with different concentrations of DND(ξ+) and DND(ξ-) (Fig. 8) show that in the case of DND with a positive charge, there is a significant change in the morphology of the composites compared with the original GO material. Already in the case of composites with the lowest DND content, the formation of filaments from GO sheets is observed (Fig. 8, *e*). With increase in the mass fraction of DNDs in the composite, the fraction of „rolled up" GO sheets increases, as well as the thickening of the filaments.

In the case of GO−DND(ξ-) composites, GO sheets do not roll up into filaments even at the highest DND concentration (Fig. 8, *d*). The only noticeable change is the structure densification due to a denser coating of GO sheets with nanodiamonds.

Magnified SEM images of the surface of GO sheets coated with DND (Fig. 9) show that in the case of GO−DND(ξ-) composites, nanodiamonds aggregate on the surface of the sheets, forming areas with dense filling. In the case of GO−DND(ξ+) composites, nanodiamonds are more uniformly distributed over the surface of the GO sheet in the form of individual weakly aggregated particles.

Fig. 10 shows the results of the estimation of the specific surface area (SSA) by the BET method. The

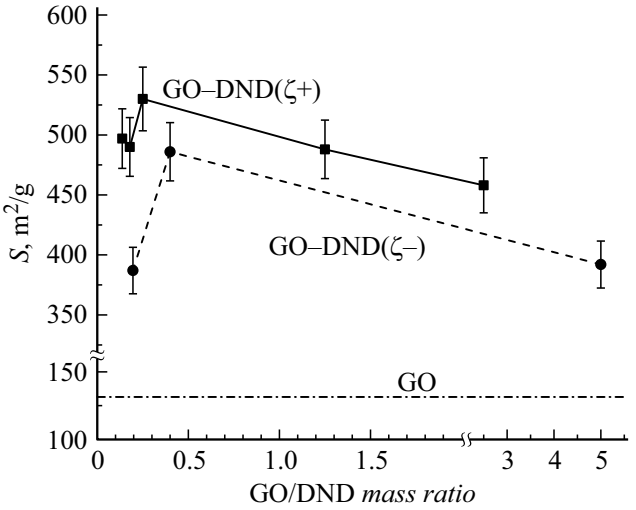

Figure 10. Specific surface area of composites in the form of aerogels vs. mass ratio GO/DND. The dotted line shows the specific surface area of the sample without DND addition, prepared under similar conditions. The mass ratio is given before removal of excess DND.

measurements were carried out on samples subjected to annealing. However, the SEM monitoring showed that no changes in morphology were observed in aerogels after annealing; therefore, the result obtained can be analyzed on the basis of data on the structure of aerogels not subjected to temperature effects. The analysis of the SSA of composites in the form of aerogels showed that even a small addition of DND particles to graphene oxide leads to a multiple increase in SSA of aerogels. The points on the graphs correspond to the actual mass ratio of GO/DND after the mixtures washing to remove excess DND. It can be seen that SSA increase of aerogels is observed for both types of structures. However, for the structures GO−DND($\xi+$) we managed to achieve the maximum value of SSA 530 m^2/g, while for the structures GO−DND(ξ-) the maximum value was 486 m^2/g. Note that in the case of the latter, at a GO/DND mass ratio exceeding 2.5, the SSA drops to 387 m^2/g. Apparently, with insufficient amount of DND particles in the initial mixture a significant amount of GO sheets stick together is formed (which is confirmed by XRD data, Fig. 7).

3. Results and discussion

Control of the morphology of graphene platelets, GO and their derivatives with obtaining their „crumpled“ and „rolled up“ configurations is currently one of the approaches to the formation of graphene-based electrode materials for energy storage systems, biofuel cells, applications in the field of catalysis and for the manufacture of adsorbents [48,50,51]. For this purpose, approaches are used to control the colloidal stability of GO suspensions by adding salts [50], soft controlled reduction of graphene oxide [47]. In the latter case, due to a gradual reduction in the number of functional groups in graphene oxide and, as a consequence, decrease in the contribution of Coulomb forces, the time occurs when the van der Waals forces become comparable with the Coulomb forces opposing them, which are responsible for the high stability of GO in water.

In the present paper the control of the morphology of graphene layers and the production of „rolled up“ GO sheets is implemented not through a complex strategy of gradual reduction of graphene oxide, but through a simpler and more Facile approach based on the introduction of DND($\xi+$) nanoparticles. Given the mutual compensation of DND($\xi+$) and GO(ξ-) charges, the electrostatic repulsion of particles responsible for colloidal stability disappears, and heterocoagulation occurs. As a result, graphene sheets roll up as the only thermodynamically favorable behavior of such a system. However, in contrast to the controlled reduction of GO, obtaining the structure based on the addition of DND nanoparticles is easier to implement in practice. Moreover, DND($\xi+$) particles play an additional role of „spacer“ for GO layers, preventing the formation of multilayer regions and maintaining the interlayer distance in structures based on this nanocomposite in the range of 4−5 nm, which is optimal value for the transport of organic molecules and metal ions for further practical application in the field of catalysis electrochemistry. The synthesis strategy consists not only in choosing detonation diamond nanoparticles as the spacer, but mainly in observing a specially developed protocol for mixing the components that form the composite: with constant stirring, a suspension of GO and a hydrosol of DND particles are simultaneously fed into water until the desired mass ratio of these components is reached in the final composite. This approach makes it possible to avoid undesirable stacking of GO layers and aggregation of DND particles, which may prevent the obtaining of composites.

The results obtained demonstrate that the approach to fabricate nanostructured composites based on graphenes and DNDs makes it possible not only to obtain „rolled up“ GO sheets, but also to control the morphology of the resulting structure by choosing the DND type. If the addition of DND($\xi+$) suspension to GO suspension leads to heterocoagulation and roll up of sheets, then the addition of a DND(ξ-) suspension leads to the formation of more lamellar structures due to the preservation of electrostatic repulsion between separate sheets, and local areas of a single sheet. As the TEM and SAXS data show, DND($\xi+$) particles are more uniformly distributed over the GO sheet, while in the case of DND(ξ-) the particles are clustered in the non-oxidized GO regions namely sp^2-domains. At the same time, the combination of data from laser diffraction, spectrophotometry, laser Doppler electrophoresis, and small-angle X-ray scattering for composites in the form of suspensions allows us to assume that, regardless of the sign of the zeta potential of DND particles, there is „saturation effect“ of the structure, appearing in a limited number of DND particles that can strongly bind to GO sheets

and it was shown that for DND($\xi+$) and DND(ξ-) the limiting concentration of DND particles differs significantly. Just because of the saturation effect the excess DND is washed out by simple centrifugation, and in the case of GO−DND($\xi+$) the structures with a larger fraction of separated GO sheets are predominantly formed, while in the case of GO−DND(ξ-) — structures with a lower fraction of separated sheets and sticky sheets of GO without the introduction of DND at are being assembled. Since only limited number of DND($\xi+$) can be bound to a given amount of GO, it is expected that the SSA of structures of the GO−DND($\xi+$) type with mGO/mDND < 0.5 are also in close ranges. Nevertheless, varying mGO/mDND in the initial mixture, it is possible to reach a different value of the total zeta potential and, as a consequence, a different degree of deformation of graphene oxide sheets during lyophilization and aerogel formation, and hence a different SSA.

Separately, note that the acquired results once again demonstrated the effectiveness of the SAXS method for studying nanocomposite structures based on GO and carbon nanoparticles, such as GO−DND($\xi+$) and GO−DND(ξ-) [39] in the form of suspensions. Even more unique SAXS results were obtained for composites in the form of aerogels. Their originality lies in the numerical description of the morphology of the structures, which makes it possible to compare them with the mechanisms of folding of graphene sheets discussed in the literature [52]. Obtaining data on the nano- and microstructure of such systems when they are in liquid medium before fabricating and studying coatings (multilayer films) and aerogels based on them allows us to expand the fundamental understanding of the processes of particles restructuring during deposition (aerosol, spin-coating or other) and lyophilization, to develop practical approaches to obtaining such structures with a given morphology.

Conclusion

In this paper composites in the form of aqueous suspensions and aerogels based on GO and DND with different signs of the zeta potential (DND($\xi+$) and DND(ξ-)) are fabricated and examined. It is shown that, despite the fundamental possibility of forming both GO−DND($\xi+$) systems and GO−DND(ξ-) systems, the use of DND with positive zeta potential advances the formation of a more uniform composite („sandwich structure").

Furthermore, the fundamental difference in the morphology of the GO−DND($\xi+$) and GO−DND(ξ-) structures is shown, which is explained by different mechanisms of coagulation at the stage of mixtures formation. It is demonstrated and explained in terms of the electrophoretic mobility of nanoparticles that the use of DND($\xi+$) makes it possible to form composites in the form of aerogels with a greater proportion of separated graphene oxide sheets, which, under conditions of mutual charge compensation, leads to twisting of graphene oxide sheets in the final structure and to a significant increase in its specific surface area.

Funding

The experiment setting, the synthesis and primary characterization of the GO suspension and DND hydrosols, as well as the study of the properties of colloidal solutions were carried out within the framework of state case studies of Ioffe Physical & Technical Institute (topic № 0040-2019-0013, „Physical and chemical foundations of the technology of new functional materials based on carbon nanostructures").

The synthesis of aerogels and the characterization of their specific surface by the BET method were carried out within the framework of the Basic Research Programs of the Russian Academy of Sciences (project № 1021051101696-3-1/4/3 and project № 122040400099-5).

The study of composites by the SAXS method using a synchrotron radiation source of the National Research Center of „Kurchatov Institute" was carried out within the framework of project supported by the Ministry of Science and Higher Education of the Russian Federation (Agreement № 075-15-2021-1349).

Structural studies were carried out using the equipment of the Federal Center of Collective Use „Materials science and diagnostics in advanced technologies".

Conflict of interest

The authors declare that they have no conflict of interest.

References

[1] R.K. Singh, R. Kumar, D.P. Singh. RSC Adv., **6**, 64993 (2016). DOI: 10.1039/C6RA07626B
[2] G. Gorgolis, C. Galiotis. 2D Mater., **4**, 032001 (2017). DOI: 10.1088/2053-1583/aa7883
[3] Y. Cheng, S. Zhou, P. Hu, G. Zhao, Y. Li, X. Zhang, W. Han. Sci. Rep., **7**, 1439 (2017). DOI: 10.1038/s41598-017-01601-x
[4] J. Mao, J. Iocozzia, J. Huang, K. Meng, Y. Lai, Z. Lin. Energy Environ. Sci., **11**, 772 (2018). DOI: 10.1039/C7EE03031B
[5] H.-Y. Mi, X. Jing, A.L. Politowicz, E. Chen, H.-X. Huang, L.-S. Turng. Carbon N.Y., **132**, 199 (2018). DOI: 10.1016/j.carbon.2018.02.033
[6] J.-Y. Hong, E.-H. Sohn, S. Park, H.S. Park. Chem. Eng. J., **269**, 229 (2015). DOI: 10.1016/j.cej.2015.01.066
[7] Z. Han, Z. Tang, S. Shen, B. Zhao, G. Zheng, J. Yang. Sci. Rep., **4**, 5025 (2015). DOI: 10.1038/srep05025
[8] S.P. Lonkar, A.A. Abdala. J. Thermodyn. Catal., **5** (2), (2014). DOI: 10.4172/2157-7544.1000132
[9] Y. Huang, J. Liang, Y. Chen. Small., **8**, 1805 (2012). DOI: 10.1002/smll.201102635
[10] A. González, E. Goikolea, J.A. Barrena, R. Mysyk. Renew. Sustain. Energy Rev., **58**, 1189 (2016). DOI: 10.1016/j.rser.2015.12.249

[11] Y. Wang, Z. Shi, Y. Huang, Y. Ma, C. Wang, M. Chen, Y. Chen. J. Phys. Chem. C, **113**, 13103 (2009). DOI: 10.1021/jp902214f
[12] S. Stankovich, D.A. Dikin, R.D. Piner, K.A. Kohlhaas, A. Kleinhammes, Y. Jia, Y. Wu, S.T. Nguyen, R.S. Ruoff. Carbon N.Y., **45**, 1558 (2007). DOI: 10.1016/j.carbon.2007.02.034
[13] Y. Chen, X. Zhang, P. Yu, Y. Ma. J. Power Sources, **195**, 3031 (2010). DOI: 10.1016/j.jpowsour.2009.11.057
[14] Y. Gu, Y. Xu, Y. Wang. ACS Appl. Mater. Interfaces, **5**, 801 (2013). DOI: 10.1021/am3023652
[15] Y. Wang, Y. Wu, Y. Huang, F. Zhang, X. Yang, Y. Ma, Y. Chen. J. Phys. Chem. C, **115**, 23192 (2011). DOI: 10.1021/jp206444e
[16] J. Hernández-Ferrer, A.M. Benito, W.K. Maser, E. García-Bordejé. Catalysts, **11**, 1404 (2021). DOI: 10.3390/catal11111404
[17] P. Arabkhani, A. Asfaram. J. Hazard. Mater., **384**, 121394 (2020). DOI: 10.1016/j.jhazmat.2019.121394
[18] Q. Wang, N. Plylahan, M.V. Shelke, R.R. Devarapalli, M. Li, P. Subramanian, T. Djenizian, R. Boukherroub, S. Szunerits. Carbon N.Y., **68**, 175 (2014). DOI: 10.1016/j.carbon.2013.10.077
[19] Y. Sun, Q. Wu, Y. Xu, H. Bai, C. Li, G. Shi. J. Mater. Chem., **21**, 7154 (2011). DOI: 10.1039/c0jm04434b
[20] A.E. Aleksenskii. *Technology of Preparation of Detonation Nanodiamond*, in: A.Y. Vul', O.A. Shenderova (ed.), *Detonation Nanodiamonds: Science and Applications*, 1st ed. (Pan Stanford Publishing, Singapore, 2014), p. 37–73.
[21] O.A. Williams, J. Hees, C. Dieker, W. Jäger, L. Kirste, C.E. Nebel. ACS nano, **4**, 4824 (2010). DOI: 10.1021/nn100748k
[22] A.E. Aleksenskiy, E.D. Eydelman, A.Y. Vul'. Nanosci. Nanotechnol. Lett., **3**, 68 (2011). DOI: 10.1166/nnl.2011.1122
[23] B. Konkena, S. Vasudevan. J. Phys. Chem. Lett., **3**, 867 (2012). DOI: 10.1021/jz300236w
[24] W.S. Hummers, R.E. Offeman. J. Am. Chem. Soc., **80**, 1339 (1958). DOI: 10.1021/ja01539a017
[25] A.E. Aleksenskii, A.Y. Vul, S.V. Konyakhin, K.V. Reich, L.V. Sharonova, E.D. Eidel'man. Phys. Solid State, **54**, 578 (2012). DOI: 10.1134/S1063783412030031
[26] A.Y. Vul, E.D. Eydelman, L.V. Sharonova, A.E. Aleksenskiy, S.V. Konyakhin. Diam. Relat. Mater., **20**, 279 (2011). DOI: 10.1016/j.diamond.2011.01.004
[27] G.S. Peters, O.A. Zakharchenko, P.V. Konarev, Y.V. Karmazikov, M.A. Smirnov, A.V. Zabelin, E.H. Mukhamedzhanov, A.A. Veligzhanin, A.E. Blagov, M.V. Kovalchuk. Nucl. Instruments Methods Phys. Res. Sect. A, **945**, 162616 (2019). DOI: 10.1016/j.nima.2019.162616
[28] G.S. Peters, Y.A. Gaponov, P.V. Konarev, M.A. Marchenkova, K.B. Ilina, V.V. Volkov, Y.V. Pisarevsky, M.V. Kovalchuk. Nucl. Instruments Methods Phys. Res. Sect. A, **1025**, 166170 (2022). DOI: 10.1016/j.nima.2021.166170
[29] M.K. Rabchinskii, S.D. Saveliev, S.A. Ryzhkov, E.K. Nepomnyashchaya, S.I. Pavlov, M.V. Baidakova, P.N. Brunkov. J. Phys. Conf. Ser., **1695**, 012070 (2020). DOI: 10.1088/1742-6596/1695/1/012070
[30] P.V. Kumar, N.M. Bardhan, S. Tongay, J. Wu, A.M. Belcher, J.C. Grossman. Nat. Chem., **6**, 151 (2014). DOI: 10.1038/nchem.1820
[31] K. Erickson, R. Erni, Z. Lee, N. Alem, W. Gannett, A. Zettl. Adv. Mater., **22**, 4467 (2010). DOI: 10.1002/adma.201000732
[32] J. Teixeira. J. Appl. Crystall., **21**, 781 (1988). DOI: 10.1107/S0021889888000263
[33] P.W. Schmidt. J. Appl. Crystall., **24**, 414 (1991). DOI: 10.1107/S0021889891003400
[34] E.G. Iashina, S.V. Grigoriev. J. Surf. Investig. X-Ray, Synchrotron Neutron Tech., **11**, 897 (2017). DOI: 10.1134/S1027451017040334
[35] Y.V. Kulvelis, M.K. Rabchinskii, A.T. Dideikin, A.D. Trofimuk, A.V. Shvidchenko, D.A. Kirilenko, M.V. Gudkov, A.I. Kuklin. J. Surf. Investig. X-Ray, Synchrotron Neutron Tech., **15**, 896 (2021). DOI: 10.1134/S1027451021050062
[36] V. Lebedev, Y. Kulvelis, A. Kuklin, A. Vul. Condens. Matter, **1**, 10 (2016). DOI: 10.3390/condmat1010010
[37] A.Y. Vul, E.D. Eidelman, A.E. Aleksenskiy, A.V. Shvidchenko, A.T. Dideikin, V.S. Yuferev, V.T. Lebedev, Y.V. Kul'velis, M.V. Avdeev. Carbon N.Y., **114**, 242 (2017). DOI: 10.1016/j.carbon.2016.12.007
[38] O.V. Tomchuk, M.V. Avdeev, L.A. Bulavin. Journal of Surface Investigation: X-ray, Synchrotron and Neutron Techniques, **14**, S231 (2020). DOI: 10.1134/S1027451020070484
[39] A.S. Barnard, S.P. Russo, I.K. Snook, Structural relaxation and relative stability of nanodiamond morphologies, Diamond and Related Materials. **12**, 1867 (2003). DOI: 10.1016/S0925-9635(03)00275-9.
[40] A.T. Dideikin, A.E. Aleksenskii, M.V. Baidakova, P.N. Brunkov, M. Brzhezinskaya, V.Yu. Davydov, V.S. Levitskii, S.V. Kidalov, Yu.A. Kukushkina, D.A. Kirilenko, V.V. Shnitov, A.V. Shvidchenko, B.V. Senkovskiy, M.S. Shestakov, A.Ya. Vul'. Carbon, **122**, 737 (2017). DOI: 10.1016/j.carbon.2017.07.013
[41] O.V. Tomchuk, L.A. Bulavin, V.L. Aksenov, V.M. Garamus, O.I. Ivankov, A.Y. Vul', A.T. Dideikin, M.V. Avdeev. J. Appl. Cryst., **41**, 642 (2014). DOI: 10.1107/S1600576714001216
[42] K. Manalastas-Cantos, P.V. Konarev, N.R. Hajizadeh, A.G. Kikhney, M.V. Petoukhov, D.S. Molodenskiy, A. Panjkovich, H.D.T. Mertens, A. Gruzinov, C. Borges, C.M. Jeffries, D.I. Svergun, D. Franke. J. Appl. Crystallogr., **54**, 343 (2021). DOI: 10.1107/S1600576720013412
[43] B.E. Warren. Phys. Rev., **59**, 693 (1941). DOI: 10.1103/PhysRev.59.693
[44] D.A. Kurdyukov, D.A. Eurov, M.K. Rabchinskii, A.V. Shvidchenko, M.V. Baidakova, D.A. Kirilenko, S.V. Koniakhin, V.V. Shnitov, V.V. Sokolov, P.N. Brunkov, A.T. Dideikin, Y.M. Sgibnev, L.Y. Mironov, D.A. Smirnov, A.Y. Vul', V.G. Golubev. Nanoscale, **10**, 13223 (2018). DOI: 10.1039/C8NR01900B
[45] M.K. Rabchinskii, S.A. Ryzhkov, D.A. Kirilenko, N.V. Ulin, M.V. Baidakova, V.V. Shnitov, S.I. Pavlov, R.G. Chumakov, D.Y. Stolyarova, N.A. Besedina, A.V. Shvidchenko, D.V. Potorochin, F. Roth, D.A. Smirnov, M.V. Gudkov, M. Brzhezinskaya, O.I. Lebedev, V.P. Melnikov, P.N. Brunkov. Sci. Rep., **10**, 6902 (2020). DOI: 10.1038/s41598-020-63935-3
[46] Y. Xue, L. Zhu, H. Chen, J. Qu, L. Dai. Carbon N.Y., **92**, 305 (2015). DOI: 10.1016/j.carbon.2015.04.046
[47] A.E. Aleksenskii. *Technology of Preparation of Detonation Nanodiamond*, in: A.Y. Vul', O.A. Shenderova (ed.). *Detonation Nanodiamonds*, (Jenny Stanford Publishing, N.Y., 2014), p. 51–86. DOI: 10.1201/b15541-4
[48] K. Iakoubovskii, M.V. Baidakova, B.H. Wouters, A. Stesmans, G.J. Adriaenssens, A.Y. Vul', P.J. Grobet. Diam. Relat. Mater., **9**, 861 (2000). DOI: 10.1016/S0925-9635(99)00354-4

[49] K.A. Shiyanova, M.V. Gudkov, M.K. Rabchinskii, L.A. Sokura, D.Y. Stolyarova, M.V. Baidakova, D.P. Shashkin, A.D. Trofimuk, D.A. Smirnov, I.A. Komarov, V.A. Timofeeva, V.P. Melnikov. Nanomaterials, **11**, 915 (2021). DOI: 10.3390/nano11040915
[50] M. Nazarian-Samani, H.-K. Kim, S.-H. Park, H.-C. Youn, D. Mhamane, S.-W. Lee, M.-S. Kim, J.-H. Jeong, S. Haghighat-Shishavan, K.-C. Roh, S.F. Kashani-Bozorg, K.-B. Kim. RSC Adv., **6**, 50941 (2016). DOI: 10.1039/C6RA07485E
[51] D. Chen, X. Liu, H. Nie. J. Colloid Interface Sci., **530**, 46 (2018). DOI: 10.1016/j.jcis.2018.06.051
[52] Z. Xu, B. Zheng, J. Chen, C. Gao. Chem. Mater., **26**, 6811 (2014). DOI: 10.1021/cm503418h